Review of Scientific Instruments ARTICLE pubs.aip.org/aip/rsi

Integration of conventional surface science techniques with surface-sensitive azimuthal and polarization dependent femtosecond-resolved sum frequency generation spectroscopy

Cite as: Rev. Sci. Instrum. 95, 063903 (2024); doi: 10.1063/5.0205278
Submitted: 25 February 2024 • Accepted: 15 May 2024 •
Published Online: 6 June 2024

Zhipeng Huang,[a] Tobias Roos, Yujin Tong, and R. Kramer Campen [b]

AFFILIATIONS

Faculty of Physics and Center for Nanointegration (CENIDE), University of Duisburg-Essen, Lotharstr. 1, 47057 Duisburg, Germany

[a]Author to whom correspondence should be addressed: zhipeng.huang@uni-due.de
[b]Email: richard.campen@uni-due.de

ABSTRACT

Experimental insight into the elementary processes underlying charge transfer across interfaces has blossomed with the wide-spread availability of ultra-high vacuum (UHV) setups that allow the preparation and characterization of solid surfaces with well-defined molecular adsorbates over a wide range of temperatures. Within the last 15 years, such insights have extended to charge transfer heterostructures containing solids overlain by one or more atomically thin two dimensional materials. Such systems are of wide potential interest both because they appear to offer a path to separate surface reactivity from bulk chemical properties and because some offer completely novel physics, unrealizable in bulk three dimensional solids. Thick layers of molecular adsorbates or heterostructures of 2D materials generally preclude the use of electrons or atoms as probes. However, with linear photon-in/photon-out techniques, it is often challenging to assign the observed optical response to a particular portion of the interface. We and prior workers have demonstrated that by full characterization of the symmetry of the second order nonlinear optical susceptibility, i.e., the $\chi^{(2)}$, in sum frequency generation (SFG) spectroscopy, this problem can be overcome. Here, we describe an UHV system built to allow conventional UHV sample preparation and characterization, femtosecond and polarization resolved SFG spectroscopy, the azimuthal sample rotation necessary to fully describe $\chi^{(2)}$ symmetry, and sufficient stability to allow scanning SFG microscopy. We demonstrate these capabilities in proof-of-principle measurements on CO adsorbed on Pt(111) and on the clean Ag(111) surface. Because this setup allows both full characterization of the nonlinear susceptibility and the temperature control and sample preparation/characterization of conventional UHV setups, we expect it to be of great utility in the investigation of both the basic physics and applications of solid, 2D material heterostructures.

I. INTRODUCTION

Understanding the properties of solid surfaces and their molecular adsorbates is important for designing better catalysts, developing new materials, and understanding elemental cycling in the environment.[1,2] Much physical insight into such systems has been gained over the last sixty years by the study of well-defined single crystalline solids in contact with small numbers of adsorbed molecules in ultra-high vacuum (UHV). Under UHV conditions, surfaces are now routinely characterized using electron-based [e.g., Low Energy Electron Diffraction (LEED),[3] Auger Electron Spectroscopy (AES),[4] and electron energy loss spectroscopy[5]], atom-based [e.g., Temperature Programmed Desorption (TPD) spectroscopy[6] and helium atom scattering[7]], photon-based [e.g., Infrared Reflection Absorption Spectroscopy (IRAS)[8,9]], and scanning probe techniques.[10] Such tools offer direct insight into the

morphology and electronic structure of clean solid surfaces. Application to systems containing adsorbates further allows characterization of adsorbate structure and the thermodynamics and mechanism of ad(de)sorption. With the increasing availability of pulsed photon and electron sources, structural fluctuations in such systems have been explored on timescales ranging from femto- to microseconds.[11–13]

Over the last several decades, it has become clear that the properties of solid surfaces in contact with other condensed phases may differ dramatically from the same solids in contact with gases.[14] However, because the mean free paths of electrons and atoms in condensed matter are $\lesssim$ nm, such systems are generally only amenable to characterization by scanning probe or photon based techniques.[15] Unfortunately, linear optical approaches, e.g., infrared or x-ray absorption, are inherently bulk sensitive. This sensitivity makes it challenging, for example, to extract the spectral response of molecular adsorbates at a solid surface in the presence of 10^{10} more of the same molecule in an adjoining bulk liquid phase. Even-order nonlinear optical techniques, e.g., sum and difference frequency generation (SFG and DFG) spectroscopy, are interface-specific in the dipole approximation.[16] Therefore, these approaches, in their vibrationally or electronically resonant variants, are interface specific analogs of bulk sensitive Infrared (IR) or UV/Vis absorption.[17–19] Because SFG/DFG spectroscopies are photon-in/photon-out, they are equally applicable to both solid/vacuum, solid/solid, and solid/liquid interfaces.[20,21] Furthermore, because they require intense ultrashort laser pulses, they lend themselves naturally to the characterization of ultrafast dynamics at interfaces between condensed phases.[22]

SFG/DFG is interface-specific for systems with an interface between two bulk phases that is inversion symmetric and can be described in the dipole approximation.[23] For systems that meet this requirement, measurement of the SFG response offers insight into the orientation of molecular adsorbates that exceeds that available from polarization resolved infrared absorption (i.e., multiple moments of adsorbate orientational distribution and applicability to systems with low infrared reflectivity).[24,25] However, even in systems that do not meet this restriction, e.g., solids in which the bulk lattice lacks inversion symmetry or systems where the interface is charged, physical insight not available from linear optical spectroscopies is often possible. To understand why, it is fruitful to remind ourselves that linear optical techniques probe the first order linear optical susceptibility: $\chi^{(1)}$, a rank two tensor. SFG, in contrast, is a second order nonlinear optical process in which the material response is given by the second order nonlinear optical susceptibility $\chi^{(2)}$, a rank three tensor.[26] Because many of the non-zero terms in $\chi^{(2)}$ can be probed individually by detecting the change in intensity of the emitted sum frequency field when changing the polarizations or angles of the three fields or orientation of the sample, it is generally possible to experimentally characterize the symmetry of the spectral response[26,27] in a manner not possible in linear approaches.

Such characterization is important because, for many systems of interest, the symmetry of the optical response of material *at* the interface differs from that in the adjoining bulk phase. For example, bulk α-SiO_2 belongs to the D_3 point group. It is, therefore, non-inversion symmetric and thus bulk SFG active. This symmetry is necessarily decreased with any termination of the bulk lattice. As shown by Liu and Shen, these differences allow the isolation of the surface (optical) phonon response of α-quartz(001), i.e., surface metal-oxygen spectral response, even in the presence of the much larger contribution from bulk α-SiO_2.[28,29] Along similar lines, charged buried interfaces induce a field that propagates into the bulk condensed phase. For example, at a semiconductor/liquid interface, the intensity of the emitted sum frequency field is a function of both the field gradient across the semiconductor's space charge layer and the electric double layer extending into solution.[30–32] This DC field breaks inversion symmetry over its characteristic screening length in either phase, thus making all matter within this volume SFG active. A variety of groups have shown that, given knowledge of the symmetry of the $\chi^{(2)}$, one can measure the spectra associated with each portion of such interfaces. For example, at a silica/water interface, the spectrum of water hydrogen-bound to the nearby silica surface can be distinguished from those several nm away but within the adjoining electric double layer.[33,34] Viewed more generally, this body of work has clarified that for systems containing two bulk phases and an interface, multiple distinct, near-interface regions may contribute to the emitted SFG and that these regions may be distinguished experimentally by fully characterizing the symmetry of a system's $\chi^{(2)}$.

Within the last several decades much work has demonstrated that atomically thin two dimensional materials often have mechanical, optical, or electrical properties that differ dramatically from bulk phases of the same stoichiometry.[35–37] While initial interest focused on the properties of single, isolated monolayers, it has become increasingly clear that the use of such materials in devices inevitably requires placing them in contact with strongly interacting bulk phases[38] and that heterostructures composed of two (or more) atomically thin monolayers offer intriguing physics not present in isolated monolayers or either bulk phase.[39,40]

Because coulomb screening is substantially reduced in monolayers relative to bulk phases of the same stoichiometry, semiconducting 2D materials, e.g., Transition Metal Dichalcogenides (TMDCs), support excitons with dramatically increased binding energies relative to conventional semiconductors (several hundred vs tens meV). As a consequence, their optical response is for monolayers weakly interacting with substrates, dominated by excitons both in photoluminescence and absorption. Placing TMDCs on strongly interacting metal substrates quenches the photoluminescence response of excitons and makes the optical response of the monolayer TMDC challenging to observe in reflection absorption measurements (the optical response of the TMDC is partially masked by that of free electrons in the metal).[41,42]

In addition to this linear optical characterization, there has been extensive nonlinear optical, principally second harmonic generation, characterization of monolayer 2D layered materials in general and TMDCs in particular.[43,44] Taken as a whole, this work suggests that monolayer 2D materials have nonlinear optical susceptibilities similar to bulk materials typically used in nonlinear photonics applications and therefore offer intriguing possibilities for devices in unconventional geometries. They also demonstrate that the symmetry of the second order nonlinear susceptibility, i.e., the $\chi^{(2)}$, sensitively reports on strain, phase, and monolayer orientation (with respect to the laboratory reference frame).[45,46] The intensity of the emitted second harmonic field increases by >1000× when the

photon energy of either of the two incident fields or the emitted second harmonic emission is in resonance with an optically accessible transition.[26] This suggests, as recently suggested by Zhumagulov *et al.*, that the characterization of resonant $\chi^{(2)}$ symmetry should allow the quantitative description of exciton symmetry and its deviation from that of the lattice.[47]

Second harmonic generation is an energetically degenerate version of sum frequency generation, usually performed with both interactions coming from the same incident beam (and, therefore, having the same angle with respect to the sample, the same photon energy, and the same polarization). An SFG measurement with independent control over polarization, photon energy, and the incident angle of each of the two incident fields offers the maximum possible access to the different components of $\chi^{(2)}$. We have recently shown that a full polarization analysis of the SFG response of MoS_2 adsorbed on Au allows quantitative separation of the optical response of the free electrons from Au or from adsorbed MoS_2.[48] While the resulting sample shows no excitonic optical response, a correct understanding of the symmetry of the SFG signal allows the separation of the optical contribution of the MoS_2 related states from that of free electrons in Au and the quantification of substrate-induced bandgap renormalization in an all-optical configuration.[49] Characterizing charge carrier dynamics in such systems, e.g., $MoSe_2/WSe_2$ heterostructures,[50] monolayer WS_2 on Ag(111),[51] or an indium tin oxide/MoS_2/aqueous NaI solution electrochemical cell, offers similar challenges to those described earlier.[52] That is, one would like to be able to independently address each component of the interfacial system when all may contribute to the measured non-equilibrium optical response.

Four practical challenges characterize such studies. First, the production of large, i.e., >1 mm, individual flakes of 2D materials is quite challenging. As a result, studies employing nonlinear optical techniques typically require an additional optical microscope to help locate the focused laser spots on the sample. Sample stages that allow both identification of the laser spot location and precise translation would additionally offer the possibility of conducting scanning imaging on the μm length scale over which the flakes of 2D materials often vary. Second, the most straightforward way to probe the symmetry of the 2D-material's $\chi^{(2)}$ is to measure the change in the emitted SFG field as a function of sample rotation around the surface normal. Third insight into the basic physical processes that control charge carrier lifetime and relaxation mechanism (e.g., the participation of phonons) typically requires conducting temperature dependent measurements over temperature ranges >150 K. As a practical matter, such measurements require a vacuum cryostat or UHV chamber. Fourth, if one additionally wishes to characterize, for example, the interaction of a 2D-material with a molecular organic phase, ultra-high vacuum conditions and associated tools to characterize the deposited organic layer are required.

To our knowledge, while multiple studies exist that measure polarization resolution, femtosecond time resolution, and azimuthal angle dependent SFG response in a UHV chamber (with a large range of temperature control and ancillary sample creation and characterization tools available), there are no reports of a setup that combines *all* of these characteristics with the ability to image the sample with ≈50 μm spatial resolution. Such a setup is required if, for example, we are to fully understand the basic physics that control valley polarization in TMDCS as a function of substrate.

Here, we report on our newly built ultra-high vacuum setup, which combines, i.e., conventional UHV surface science sample preparation and characterization, femtosecond resolved sum frequency generation spectroscopy, and a sample manipulator that allows high precision translation and rotation of the sample. In what follows, we first demonstrate system capabilities similar to those of existing systems. We do so by preparing a pristine Pt(111) surface that has been demonstrated to be contaminant free by Auger Electron Spectroscopy (AES) and has low defect density by comparison to published Low Energy Electron Diffraction (LEED) results. After preparation, the surface is dosed with CO. CO orientation is characterized by polarization resolved vibrationally resonant sum frequency generation spectroscopy and CO adsorption energy by temperature programmed desorption. The ability to probe femtosecond resolved dynamics is demonstrated by the collection of the free induction decay of the adsorbed CO. We next demonstrate that the system allows accurate collection of azimuthal dependent SFG by collecting azimuthal angle dependent SFG from the Ag(111) surface and comparing the resulting signal's symmetry to that of the LEED pattern collected from the same sample. Finally, we show, by comparing the scanned SFG image of a roughened Ag(111) crystal with an optical micrograph collected from the same sample, that our system is capable of collecting SFG images with a spatial resolution of ≈41 μm and a spatial movement precision of 10 μm. These proof-of-principle measurements show the system offers a novel combination of existing approaches that are of particular potential utility in the characterization of the properties of charge carriers and their relaxation in 2D-materials.

II. RESULTS AND DISCUSSION

A. Description of our UHV setup

A schematic drawing of our ultra-high vacuum (UHV) setup is shown in Fig. 1. It consists of four main chambers: a load-lock chamber for sample loading, a radial distribution (UFO) chamber (PREVAC GmbH) for sample transfer, a preparation chamber for sample preparation and inspection, and the SFG chamber for sample characterization. The setup allows in-vacuum sample preparation, transfer, and characterization. The load-lock chamber has an O-ring sealed quick access door and a stainless steel frame holder for loading and storing a sample. The sample preparation chamber contains an argon ion sputtering gun (SPECS GmbH), a low energy electron diffraction/Auger electron spectroscopy instrument (SPECS GmbH), a quadrupole mass spectrometer (RGA100, Stanford Research Systems) for temperature programmed desorption spectroscopy, and a four-axis manipulator (PREVAC GmbH), which can translate the sample along the x-, y-, and z-axes and rotate it with respect to the z-. The manipulator can be cooled with liquid nitrogen to ~−120 °C and heated to a temperature of ~1100 °C by resistive or ~1400 °C by electron beam heating. An argon ion sputtering gun is used for cleaning the sample surface by bombarding it with high-voltage (i.e., 1 kV) accelerated argon ions. The sample preparation chamber is mounted with a leak valve (VAT Group AG) that enables controlled dosing of a wide range of gases. The radial distribution chamber is located at the center of the setup, contains a rotary transfer arm, and is connected with the other three chambers by gate valves (VAT Group AG), a configuration chosen so as to allow separate pumping of each chamber. This configuration allows

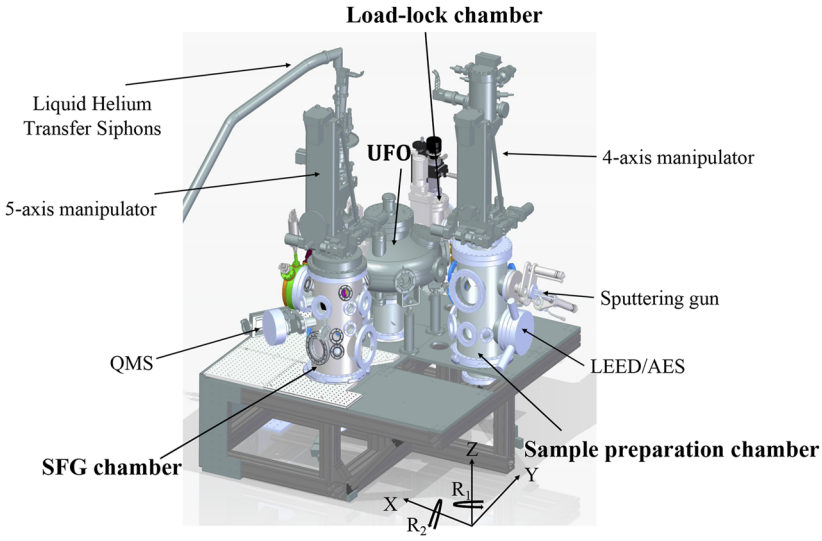

FIG. 1. Schematic drawing of the ultra-high vacuum setup. Major components of the system are labeled. See the text for details.

independent pumping of each chamber and the transfer of samples between all chambers without leaving vacuum. The SFG chamber is equipped with a quadrupole mass spectrometer (RGA200, Stanford Research Systems) for temperature programmed desorption spectroscopy and a five-axis motorized manipulator (PREVAC GmbH) that can translate the sample along the x-, y-, or z-axes and rotate it with respect to the z-axis and the sample surface normal (x- or y-axis depending on sample orientation). The sample can be cooled to −220 °C with liquid helium or −120 °C with liquid nitrogen and heated to ~1100 °C by resistive heating or ~1400 °C by electron beam heating. The SFG chamber is mounted with two independent leak valves (VAT Group AG) that enable *in situ* SFG measurements while gas dosing with controlled dosing pressures. To achieve ultra-high vacuum pressure, each chamber is evacuated by an independent oil-free turbo molecular pump (Pfeiffer Vacuum) backed by a HiCube 80 Eco turbo pumping station (Pfeiffer Vacuum). The typical pressure inside each chamber (excepting the load-lock) is $\sim 1 \times 10^{-10}$ mbar.

B. Description of our laser setup

A schematic drawing of the laser setup is shown in Fig. 2. We employ a laser system composed of a Ti:Sapphire oscillator (Vitara, Coherent) that seeds a regenerative amplifier (Legend Elite Duo HE + USP, Coherent) that delivers pulses with an energy of $6\frac{\text{mJ}}{\text{pulse}}$, a center wavelength of 800 nm, a duration of 35 fs (FWHM), and a repetition rate of 1 KHz. The amplifier's output is split into three beams. One beam with a power of ~1.8 W (1.8 mJ/pulse) pumps a commercial optical parametric amplifier (TOPAS-Prime, Light Conversion). The signal and idler beams produced by the optical parametric amplifier (OPA) are subsequently mixed in a collinear difference frequency generation scheme to generate broadband infrared (IR) femtosecond pulses, the center wavelength of which can be tuned from 2 to 13 μm. The second beam is spectrally shaped by an air-spaced etalon (SLS Optics Ltd.) to produce a narrowband 800 nm beam. To conduct vibrationally or final-state resonant SFG measurements, the infrared and narrowband 800 nm beams are spatially and temporally overlapped at the sample surface. The third beam propagating on this portion of the table is part of the 800 nm femtosecond amplifier used as a *pump* in various pump–SFG probe experiments. The 800 nm pump is straightforwardly doubled or tripled in frequency using nonlinear crystals (e.g., BaB_2O_4, LiB_3O_5, KH_2PO_4, $KTiOPO_4$, etc.) to generate alternative UV pump pulses at 400 or 267 nm.[53,54] The SFG chamber is designed so as to allow the pump beam to propagate collinearly with the narrowband 800 nm beam as shown in Fig. 2 or to pump over a range of possible angles of 0°–5° (but within the plane defined by the incident narrowband 800 and infrared). This collinear geometry makes it straightforward to conduct pump-SFG probe measurements without the need to change the SFG beam path. The relative delay between the pump pulse and the IR or narrowband 800 nm pulse is controlled by a motorized optical delay stage (GTS150, Newport Corporation) in the optical path of the pump. A $\frac{\lambda}{2}$ waveplate and a polarizer are mounted in each of these three beams to allow continuous pulse energy adjustment while maintaining a clean p- or s-polarization. The diameter of the cylindrical SFG chamber is ~30 cm, thus the focal distance of the lens for the incident three beams (pump, narrowband 800, and tunable IR) needs to be longer than 15 cm (given a sample located at the center of the chamber). Here, the incident IR beam is focused by an uncoated ZnSe lens with a focal length of 25 cm. The narrowband 800 and pump beams are focused by an N-BK7 plano-convex lens with a focal length of 40 cm. In a configuration in which all three beams enter the SFG chamber through a single viewport, a DN63CF KBr window (Torr Scientific Ltd.) is employed. The incidence angles of the IR beam and the narrowband 800 nm beam with respect to the surface normal axis in this single viewport configuration are 46.1° and 53.1°, respectively. The focus beam diameters (after projecting on the sample) of the narrowband

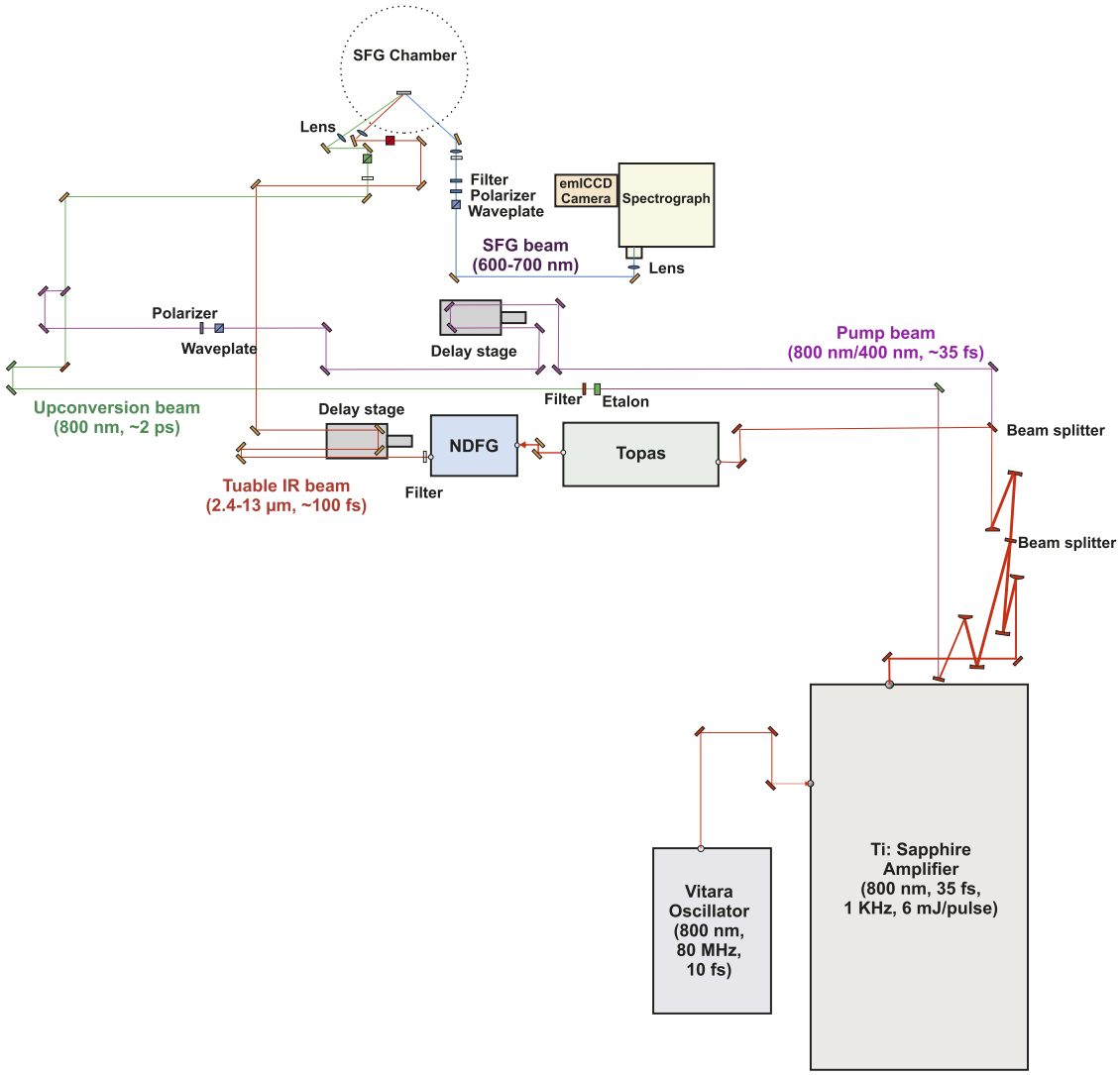

FIG. 2. Schematic drawing of the femtosecond laser setup for (time-resolved) sum frequency generation spectroscopy measurement. See the text for details.

800 and infrared beams are ~110 and 270 μm (for the long-axis), respectively. The dimensions of this spot can be readily decreased in the current setup. A lens with a focal length of 15 cm (the smallest distance compatible with the 15 cm radius of the SFG chamber) would decrease the spot size (short axis) to 41 μm. Similarly, doubling the visible beam with a telescope before focusing would allow a further decrease in spot size to 21 μm. Once the two beams are spatially and temporally overlapped on the sample surface, an SFG beam will be produced. The generated SFG beam is collimated by a 40 cm lens and then filtered by a short pass filter with a cutting wavelength of 750 nm to eliminate the narrowband at 800 nm and pump pulses. The filtered SFG beam is propagated through a polarizer to select only clean p- or s-polarized SFG emission, then rotated to p-polarization by a $\frac{\lambda}{2}$ waveplate and dispersed by a spectrograph (SpectraPro HRS-300) onto an emICCD camera (Princeton Instrument PI-MAX 4). Ensuring all SFG fields are p-polarized before entering the spectrograph removes the necessity of correcting for grating efficiencies that are a function of field polarization.[55] The polarization dependent SFG measurement is realized using different polarization combinations of the narrowband 800 nm and IR beams and detecting the generated SFG of different polarizations.

Much prior work has shown that polarization resolved detection of vibrationally resonant SFG can be used to determine the orientation of adsorbed molecules on solid surfaces and interface-induced intermolecular coupling.[56] In Sec. II C, we demonstrate this capability in our setup by examining the prototypical system CO on Pt(111) (see supplementary material for laser parameters).

C. Polarization resolved VSFG of CO on Pt(111) in UHV

Platinum (Pt) is widely employed as a catalyst for (de)hydrogenation, reduction, and oxidation reactions due to its high activity, stability, and selectivity. Reactions on Pt involving the transformation of small hydrocarbons often produce CO as an intermediate.[57,58] As a result, the adsorption of CO on Pt(111) has been extensively studied.[59,60] We prepared clean Pt(111) surfaces in the sample preparation chamber by Ar ion bombardment (with an acceleration voltage of 1000 V and filament current of 10 mA) for one hour, followed by annealing at 900 °C for 10 min with the sputtering → annealing cycle repeated five times. The heating rate to reach the annealing temperature was $\approx 300 \frac{^\circ C}{min}$, and the cooling rate was $\approx -250 \frac{^\circ C}{min}$. After these sputtering and annealing cycles, we verified that the Pt(111) surface was contaminant free by Auger electron spectroscopy [see Fig. 3(d)] and that the surface has the expected 1 × 1 LEED pattern (see supplementary material). Having verified that the sample surface was contaminant free and had the expected structure, the sample was cooled to −70 °C for CO dosing. CO dosing was performed via a leak valve. We calibrated CO surface coverage to dosing conditions by dosing for a defined time and pressure, shutting the leak valve, and collecting temperature programmed desorption (TPD) spectra. TPD spectra were collected by heating the sample at a rate of 80 °C/min and detecting the increase in CO partial pressure (as CO desorbs from the surface) with a quadrupole mass spectrometer whose tip is placed 3 mm away from the sample surface. Since the pumping speed of our UHV setup is much larger than the CO partial pressure increase due to desorption, the measured CO partial pressure is proportional to the desorption rate.[61] This measurement allows calibration of the TPD response of a CO saturated monolayer (multilayer adsorption is evident as a lower temperature feature in the TPD spectra that grows under extended dosing).

Figure 3(a) shows the TPD spectrum of CO on Pt(111) with three different CO surface coverages. Following prior workers, we assume the desorption of CO from Pt(111) during a thermal ramp has a single rate limiting step and extract the desorption energy (E_{CO}) and order (x) from the data by fitting the results with the Polanyi–Wigner equation,[6,62,63]

$$-\frac{d\Theta_{CO}}{dt} = \nu_{CO}\Theta_{CO}^{x}\exp\left(-\frac{E_{CO}}{RT}\right), \quad (1)$$

where Θ_{CO} is the surface coverage of CO and ν_{CO} is the preexponential frequency factor. We find the E_{CO} on Pt(111) to be 110 kJ/mol and the desorption to have an order of 2, consistent with previous results.[59,60] Since it is known that the saturation coverage of CO on Pt(111) in UHV at room temperature is 0.5 ML,[59,64] the integrated area of the TPD spectrum at saturated CO monolayer coverage allows quantification of surface coverage under reduced dosing. Figure 3(b) shows the LEED pattern of CO adsorbed on Pt(111) with a coverage of 0.5 ML and a probe electron beam energy of 32 eV. Figure 3(c) shows the LEEDpat[65] simulated result from

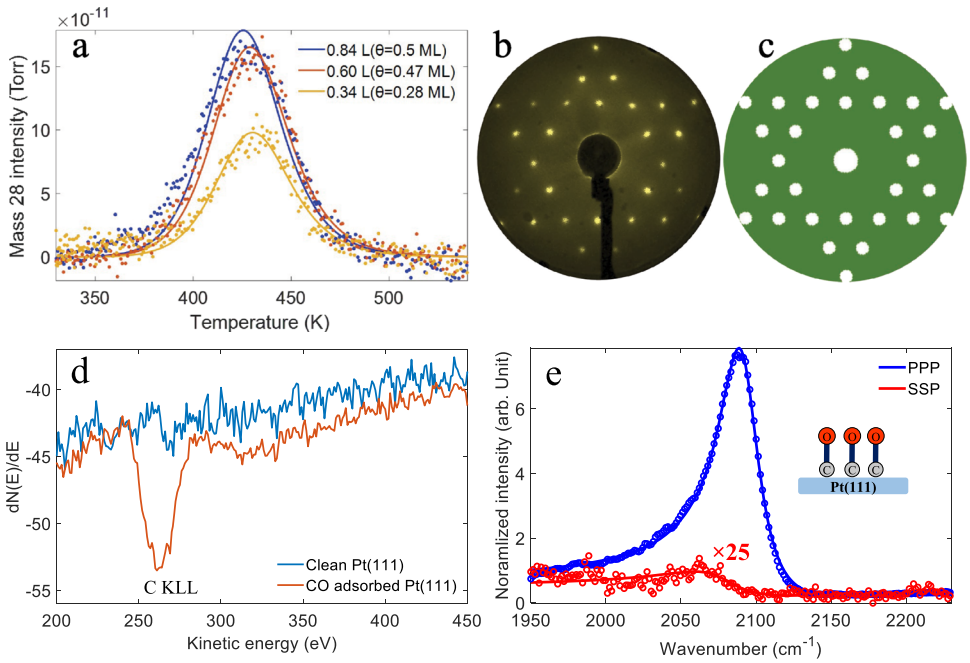

FIG. 3. (a) Temperature programmed desorption spectrum of CO chemisorbed on Pt(111) with three different CO dosing quantities: 0.84 L (blue), 0.60 L (red), and 0.34 L (orange). (b) Low energy electron diffraction pattern of CO adsorbed on Pt(111) with a coverage of 0.5 monolayer. The probe's electron beam energy is 32 eV. (c) Simulated LEED result of a $c(4 \times 2)$ adsorbed structure on a Pt(111) surface (see supplementary material for details). (d) Auger electron spectrum of a clean Pt(111) surface (blue) and a CO chemisorbed Pt(111) surface (red). (e) Vibrationally resonant sum-frequency spectrum of chemisorbed CO on Pt(111) with a coverage of 0.5 ML under *ppp* polarization (blue) and *ssp* polarization (red). See the text for details.

a c(4 × 2) adsorption structure. The calculated structure is clearly consistent with the experimental results. Viewed in real-space, a 0.5 ML coverage and c(4 × 2) adsorbate structure are consistent with a structure in which adsorbed CO molecules populate both on-top and bridge sites of Pt(111).[60] Figure 3(d) shows the Auger electron spectra of the clean Pt(111) surface (blue) and the same surface with a half monolayer of adsorbed CO (red). Clearly, the C KLL peak,[66] centered at around 262 eV, appears only after CO dosing.

Collecting vibrationally resonant sum frequency spectra requires spatially and temporally overlapping incident infrared and visible fields at a sample surface and detecting the intensity of the emitted field at the sum of the two incident frequencies. Figure 3(e) shows the normalized vibrational sum frequency generation (VSFG) spectrum [clean Pt(111) was used as the reference sample to normalize the spectra] collected from a sample with a half-monolayer (Θ = 0.5 ML) CO adsorbed on Pt(111) collected under the *ppp* (blue) and *ssp* (red) polarization conditions measured in the SFG chamber (where *ssp* indicates s-polarized SFG, *s*-polarized narrowband 800 nm, and *p*-polarized IR. *s* indicates ⊥ to the incident plane and *p* ∥). On-top adsorbed CO on a wide variety of metals is known to be resonant at the infrared photon energies we employ.[15,67,68]

The ratio of vibrationally resonant SFG intensity measured under the *ppp* to that measured under the *ssp* condition, i.e., $\frac{I_{sf,ppp}}{I_{sf,ssp}}$, is a function of the orientation of CO on the Pt(111) surface and the ratio of components of the hyperpolarizability tensor, i.e., the second order molecular response $\beta^{(2)}$.[24,26,69] While $\beta^{(2)}$ is a function of the local environment, particularly near resonant optical transitions, its value is rarely accessible in condensed molecular phases or at interfaces, making it challenging to separate the contribution of orientation and electronic structure in the observed sum frequency response.[24,26,27,70] As noted earlier, prior work has demonstrated that the sharply resolved c(4 × 2) LEED pattern of CO adsorbed on Pt(111) strongly suggests that atop adsorbed CO is oriented normal to the Pt(111) surface.[71–74] Therefore, this system offers a relatively rare opportunity to elucidate the $\beta^{(2)}$ for CO adsorbed on Pt(111) at a coverage of 0.5 ML. Understanding how the macroscopic observables are related to microscopic structure requires a review of the physical basis of the VSFG response.[24,26]

The VSFG spectrum of CO adsorbed on Pt(111) shown in Fig. 3(e) results from spatially and temporally overlapping a narrowband pulse train in the visible and an infrared pulse train in the mid-infrared,

$$I_{sf}(\omega_{sfg}) \propto \left|\chi^{(2)}_{eff}\right|^2 I_{vis}(\omega_{vis}) I_{ir}(\omega_{ir}), \tag{2}$$

where I_{sf} is the intensity of the emitted SFG field (and is a function of photon energy, i.e., ω_{SFG}), I_{vis} is the intensity of the narrowband visible up-conversion pulse (and is a function of ω_{vis}), and I_{ir} is the intensity of the incident infrared field (and is a function of ω_{ir}). $\chi^{(2)}_{eff}$, the *effective* second order macroscopic susceptibility, is the sum of nonresonant and vibrationally resonant transitions. If each vibrational transition is only homogeneously broadened, it can be written as

$$\chi^{(2)}_{eff}(\omega_{ir}) = \chi^{(2)}_{nr} + \chi^{(2)}_{res} = A_{nr} e^{i\phi_{NR}} + \sum_q \frac{A_q}{\omega_{ir} - \omega_q + i\Gamma_q}, \tag{3}$$

where $\chi^{(2)}_{nr}$ is the nonresonant (often assigned to the distant tail of high energy optically accessible transitions[75]) and $\chi^{(2)}_{res}$ is the resonant part of the second-order nonlinear susceptibility. A_{nr} is the amplitude of the nonresonant background, and ϕ_{NR} is the phase. A_q, ω_q, and Γ_q are the amplitude, resonant frequency, and damping coefficient of the qth vibrational mode, respectively.

$\chi^{(2)}_{eff}$ is *effective* in Eq. (2) in that it is also a function of the polarizations or angles (with respect to the surface normal) of the incident and emitted fields. Disentangling these parameters gives

$$\begin{aligned}\chi^{(2)}_{eff,ppp} = &-L_{XX}(\omega_{sfg}) L_{XX}(\omega_{vis}) L_{ZZ}(\omega_{ir}) \cos\alpha_{sfg} \cos\alpha_{vis} \sin\alpha_{ir} \chi^{(2)}_{XXZ} \\ &- L_{XX}(\omega_{sfg}) L_{ZZ}(\omega_{vis}) L_{XX}(\omega_{ir}) \cos\alpha_{sfg} \sin\alpha_{vis} \cos\alpha_{ir} \chi^{(2)}_{XZX} \\ &+ L_{ZZ}(\omega_{sfg}) L_{XX}(\omega_{vis}) L_{XX}(\omega_{ir}) \sin\alpha_{sfg} \cos\alpha_{vis} \cos\alpha_{ir} \chi^{(2)}_{ZXX} \\ &+ L_{ZZ}(\omega_{sfg}) L_{ZZ}(\omega_{vis}) L_{ZZ}(\omega_{ir}) \sin\alpha_{sfg} \sin\alpha_{vis} \sin\alpha_{ir} \chi^{(2)}_{ZZZ},\end{aligned} \tag{4}$$

$$\chi^{(2)}_{eff,ssp} = L_{YY}(\omega_{sfg}) L_{YY}(\omega_{vis}) L_{ZZ}(\omega_{ir}) \sin\alpha_{ir} \chi^{(2)}_{YYZ}, \tag{5}$$

where α_i denotes the angle of the ith beam with respect to the surface normal. $\chi^{(2)}_{IJK}$ is the macroscopic second-order susceptibility in laboratory coordinates, in which Z is the surface normal and all beams propagate in the X–Z plane. $L_{II}(\omega_i)$ denotes the Fresnel factor at frequency (ω_i) and corrects for linear optical effects on the interfacial nonlinear optical response. The Fresnel factors can be written as[24,26]

$$\begin{aligned}L_{XX}(\omega) &= \frac{2n_{vac}(\omega)\cos\gamma}{n_{vac}(\omega)\cos\gamma + n_{Pt}(\omega)\cos\alpha}, \\ L_{YY}(\omega) &= \frac{2n_{vac}(\omega)\cos\alpha}{n_{vac}(\omega)\cos\alpha + n_{Pt}(\omega)\cos\gamma}, \\ L_{ZZ}(\omega) &= \frac{2n_{vac}(\omega)\cos\alpha}{n_{vac}(\omega)\cos\gamma + n_{Pt}(\omega)\cos\alpha}\left(\frac{n_{vac}(\omega)}{n'(\omega)}\right)^2,\end{aligned} \tag{6}$$

where n_{vac}, n_{Pt}, and n' are the refractive indices of the vacuum, single crystal, and interfacial layer, respectively. γ is the refracted angle $[n_{vac}(\omega)\sin\alpha = n_{Pt}(\omega)\sin\gamma]$. We estimated n' using a modified Lorentz model,[24] $n' = n_{vac} n_{Pt} \sqrt{\frac{6+(n_{Pt})^2-(n_{vac})^2}{4(n_{Pt})^2+2(n_{vac})^2}}$. The refractive indices of the vacuum, single crystal Pt(111), and interfacial layer under the wavelengths of our experimental conditions are listed in the supplementary material (Table S1).

The macroscopic second-order susceptibility $\chi^{(2)}_{IJK}$ in laboratory coordinates is related to the microscopic hyperpolarizability tensor $\beta^{(2)}_{ijk}$ in the molecular coordinate system,

$$\chi^{(2)}_{IJK} = N_s \sum_{i,j,k} \left\langle (\hat{I}\cdot\hat{i})(\hat{J}\cdot\hat{j})(\hat{K}\cdot\hat{k}) \right\rangle \beta^{(2)}_{ijk}, \tag{7}$$

where N_s is the density of molecules in the focal spot and $\langle\cdots\rangle$ indicates an ensemble average of the Euler matrix necessary to transform individual molecules into the laboratory reference frame. For CO,

a molecule with $C_{\infty v}$ symmetry around the CO bond, $\beta^{(2)}_{aac} = \beta^{(2)}_{bbc}$. Given this symmetry $\chi^{(2)}_{IJK}$ is related to $\beta^{(2)}_{ijk}$,[24,26]

$$\begin{aligned}\chi^{(2)}_{XXZ} &= \chi^{(2)}_{YYZ} = \frac{1}{2}N_s\beta^{(2)}_{ccc}\left[(1+R)\langle\cos\theta\rangle - (1-R)\langle\cos\theta\rangle^3\right],\\ \chi^{(2)}_{XZX} &= \chi^{(2)}_{ZXX} = \frac{1}{2}N_s\beta^{(2)}_{ccc}\left[(1-R)\langle\cos\theta\rangle - (1-R)\langle\cos\theta\rangle^3\right],\\ \chi^{(2)}_{ZZZ} &= N_s\beta^{(2)}_{ccc}\left[R\langle\cos\theta\rangle + (1-R)\langle\cos\theta\rangle^3\right],\end{aligned} \tag{8}$$

where θ is the orientation angle between the CO molecular axis and the surface normal, and R is the hyperpolarizability ratio ($R = \beta^{(2)}_{aac}/\beta^{(2)}_{ccc}$). A related quantity, the bond polarizability ratio (r), is often relevant in Raman spectroscopy. For isotropic systems, the measurable Raman depolarization ratio (ρ) is related to the bond polarizability ratio (r), $\rho = \frac{3}{4+5[(1+2r)/(1-r)]^2}$.[27] For molecules, such as CO, with $C_{\infty v}$ symmetry, the hyperpolarizability ratio and the bond polarizability ratio are equivalent.

Given an R measured in bulk solution, Eq. (8) allows, provided the vibrational response of CO is independent of the local environment, direct determination of interfacial CO orientation from measured VSFG spectra. This independence is, however, not generally true for interfaces of catalytic interest (e.g., CO shows a large electrochemical Stark shift[76]).

Previous workers have found an R-value for the free CO molecule from the density functional theory of 0.25.[77] In contrast, experimentally, the R-value of on-top adsorbed CO on Pt(111) has been found to be 0.6 at an electrode aqueous electrolyte interface[78] and 0.49 for multilayer CO at Pt(111) gas phase interface.[69] Both efforts calculated R from polarization dependent SFG measurements, assuming CO molecules were oriented normal to the surface. As noted earlier, the well-defined c(4 × 2) pattern we observe in LEED is strong independent evidence that CO is oriented normal to the surface for (sub)monolayer coverages of CO on Pt(111) over a wide range of temperature.[74] This system thus offers an opportunity to determine the R value of interfacial CO without making assumptions about orientation.

As is perhaps obvious from Eqs. (3)–(5), extracting either R or θ from arbitrary VSFG spectra measured under the *ppp* and *ssp* polarization conditions is not generally possible. Taking the *ratio* of $I_{sf,ppp}$ to $I_{sf,ssp}$ helps, N_s cancels, but leaves the problem of correctly describing the four different possible contributions to $\chi^{(2)}_{eff,ppp}$. Because our measured spectrum has only a single resonance and $\chi^{(2)}_{res} \gg \chi^{(2)}_{nr}$, substantial simplifications are possible. On the LHS of Eq. (4), $\chi^{(2)}_{eff,ppp} \approx \chi^{(2)}_{res,ppp}$, and both the LHS and the RHS can be evaluated at the single maximum measured intensity with no introduction of error. Pursuing such an approach and making a similar approximation in analyzing the *ssp* spectra, the measured $\frac{I_{sf,ppp}}{I_{sf,ssp}}$ = 182.6, implying R = 0.07. The orientation of on-top adsorbed CO on Pd(100) is known to deviate from normally oriented with multilayer formation due to adsorbate/adsorbate interaction.[79] The lower R we observe relative to that Li *et al.*[69] inferred under high CO coverage is thus consistent with a scenario in which R is CO coverage dependent or orientation at higher pressures deviates from normal. Similarly, the lower R we observe relative to that inferred by Baldelli *et al.*,[78] assuming CO is normally oriented at a Pt(111) working electrode, is consistent with the scenario in which R depends on the local environment, i.e., in this case, electrolyte or bias, or CO orientation is non-normally oriented at the electrochemical interface. Resolving this discrepancy for both environments is important for quantitatively inferring interfacial structure from nonlinear optical observables and is an object of current research.[80]

D. Temporal resolution of the SFG spectral response

Having confirmed that our setup offers the capability of measuring time-averaged VSFG spectra of molecular adsorbates on single crystals,[69,81,82] we next show, as initially demonstrated by previous workers,[11,22,83–86] that it also allows the resolution of energy flow dynamics on femtosecond timescales.

Figure 4 shows the spectrally integrated SFG signal derived from temporally and spatially overlapping a 35 fs 800 nm pulse (the pump beam line discussed in Sec. II B) and the IR probe beam with a center wavelength of 4725 nm as a function of the delay between the two pulses (dashed red line). Because electron relaxation in Pt is sub-10 fs and frequency independent at these photon energies, this signal is solely a function of the length and spectral shape of these two beams.[87] The FWHM of the resulting cross-correlation is 80 fs; our temporal resolution, assuming both IR and 800 nm pulses are Gaussians in the time domain, is 34 fs ($\sigma \approx \frac{FWHM}{2.355}$).

The blue points in Fig. 4 show a similar signal now collected from a Pt(111) surface prepared as indicated earlier with 0.5 monolayer of CO. Fitting the data with a single exponential (blue line in Fig. 4) quantifies the vibrational dephasing time: 1.1 ps. This result is both consistent with previous work[88] and, after Fourier transformation, yields a frequency domain bandwidth of 15 cm^{-1}. Our direct measurement of the linewidth in the frequency domain, shown in Fig. 3, yields a linewidth of 16 cm^{-1} after fitting with Eq. (3). While in principle, sampling in the time- or frequency domains offers no additional insight, in practice, the each scheme is often sensitive to different features of the spectral response.[89] The developed setup provides options to detect both of them with high precision.

As discussed in Sec. II B, the ability to resolve VSFG signals both from combining the temporally short "pump" at 800 nm and probe IR and the temporally long "probe" at 800 nm and probe

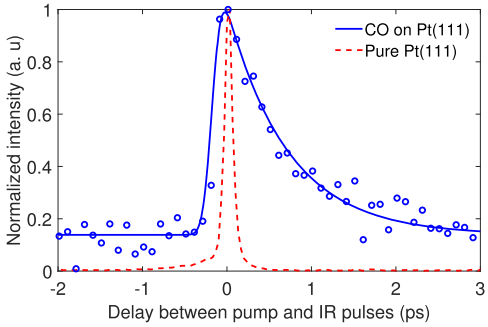

FIG. 4. The red dashed line shows the cross-correlation of the femtosecond pump beam and IR beam. The data are derived from integrating the measured sum frequency spectrum from clean Pt(111) as a function of the delay between the pump and IR pulses. The blue curve shows the vibrational dephasing dynamics of CO after IR excitation. The data are derived from integrating the measured sum frequency spectrum from 0.5 ML CO covered Pt(111) as a function of the delay between the two beams. See the text for details.

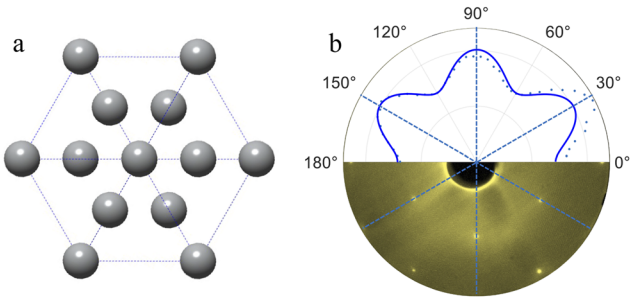

FIG. 5. (a) The Ag(111) unit cell structure. (b) Top part: Integrated sum-frequency generation spectrum of Ag(111) as a function of azimuthal angle from 0° to 180°. Bottom part: Low Energy Electron Diffraction (LEED) pattern of the Ag(111) surface collected with an electron beam energy of 145 eV. See the text for details.

IR suggests pump-probe time-resolved sum-frequency generation spectroscopy, in which either the dynamics of vibrational relaxation[84] or that of charge transfer between molecular adsorbates and the solid, initiated by the femtosecond pump pulse, should be straightforward. Such experiments are required to understand the elementary processes that underlie catalysis, solar cells, and a variety of sensing applications.[90,91]

E. The Ag(111) azimuthal dependent SFG response

Having shown that time-averaged, polarization resolved VSFG spectroscopy and femtosecond time-resolved VSFG spectroscopy are possible within our setup, we next demonstrate the possibility of measuring the polarization resolved VSFG signal as a function of azimuthal angle.

Silver (Ag) is commonly used as a catalyst for producing ethylene oxide and formaldehyde.[92,93] Solid elemental Ag has a face-centered cubic lattice.[94] Therefore, its (111) surface exhibits a hexagonal close-packed structure [as shown in Fig. 5(a)], belongs to the C_{3v} point group, has symmetry[95] and, along the surface normal, has an ABCABC stacking sequence. The characterization of the interfacial nonlinear optical response vs azimuthal angle offers the perspective of probing adsorbate orientation relative to Ag surface structure (as well as the opportunity discussed earlier to probe the SFG spectral response of TMDC monolayers at interfaces).

As discussed in Sec. II A, the SFG chamber is equipped with a high-stability motorized five-axis UHV manipulator that, in principle, should enable SFG measurements that rely on rotating or translating the sample and also require *in situ* heating or cooling of the sample. To conduct the azimuthal resolved measurement, we first prepare a clean Ag(111) sample using a sputtering annealing treatment, in which sputtering is accomplished by Ar ion bombardment (with a filament current of 10 mA and acceleration voltage of 1000 V) for one hour, followed by annealing at 600 °C for 10 min.[96,97] We found five such cycles in the sample preparation chamber to be sufficient to produce a clean, well-defined Ag(111) surface. Solid surfaces with C_{3v} symmetry have 11 nonvanishing and 5 independent hyperpolarizability tensor elements. For Ag(111), these are, i.e., $\beta^{(2)}_{bbb} = -\beta^{(2)}_{baa} = -\beta^{(2)}_{aab} = -\beta^{(2)}_{aba}$, $\beta^{(2)}_{aca} = \beta^{(2)}_{bcb}$, $\beta^{(2)}_{aac} = \beta^{(2)}_{bbc}$, $\beta^{(2)}_{caa} = \beta^{(2)}_{cbb}$, and $\beta^{(2)}_{ccc}$, where a, b, and c are the crystallographic axes.[48,98] The effective second-order nonlinear susceptibility measured under the *ppp* polarization condition, i.e., the $\chi^{(2)}_{ppp}$, is given by the following (where the c crystallographic axis is parallel to the z-axis surface normal, both incident laser beams propagate in the x-z plane, and the a–b crystallographic plane is parallel to the x-y plane of the laboratory frame),

$$\begin{aligned}\chi^{(2)}_{\mathrm{eff,ppp}} &= -L_{xx}(\omega_{sfg})L_{xx}(\omega_{vis})L_{xx}(\omega_{ir})\cos\alpha_{sfg}\cos\alpha_{vis}\cos\alpha_{ir}\chi^{(2)}_{xxx} - L_{xx}(\omega_{sfg})L_{xx}(\omega_{vis})L_{zz}(\omega_{ir})\cos\alpha_{sfg}\cos\alpha_{vis}\sin\alpha_{ir}\chi^{(2)}_{xxz}\\ &\quad -L_{xx}(\omega_{sfg})L_{zz}(\omega_{vis})L_{xx}(\omega_{ir})\cos\alpha_{sfg}\sin\alpha_{vis}\cos\alpha_{ir}\chi^{(2)}_{xzx} + L_{zz}(\omega_{sfg})L_{xx}(\omega_{vis})L_{xx}(\omega_{ir})\sin\alpha_{sfg}\cos\alpha_{vis}\cos\alpha_{ir}\chi^{(2)}_{zxx}\\ &\quad +L_{zz}(\omega_{sfg})L_{zz}(\omega_{vis})L_{zz}(\omega_{ir})\sin\alpha_{sfg}\sin\alpha_{vis}\sin\alpha_{ir}\chi^{(2)}_{zzz}\\ &= -L_{xx}(\omega_{sfg})L_{xx}(\omega_{vis})L_{xx}(\omega_{IR})\cos\alpha_{sfg}\cos\alpha_{vis}\cos\alpha_{ir}\beta_{bbb}\sin(3\varphi) - L_{xx}(\omega_{sfg})L_{xx}(\omega_{vis})L_{zz}(\omega_{ir})\cos\alpha_{sfg}\cos\alpha_{vis}\sin\alpha_{ir}\beta_{aac}\\ &\quad -L_{xx}(\omega_{sfg})L_{zz}(\omega_{vis})L_{xx}(\omega_{ir})\cos\alpha_{sfg}\sin\alpha_{vis}\cos\alpha_{ir}\beta_{aca} + L_{zz}(\omega_{sfg})L_{xx}(\omega_{vis})L_{xx}(\omega_{ir})\sin\alpha_{sfg}\cos\alpha_{vis}\cos\alpha_{ir}\beta_{caa}\\ &\quad +L_{zz}(\omega_{sfg})L_{zz}(\omega_{vis})L_{zz}(\omega_{ir})\sin\alpha_{sfg}\sin\alpha_{vis}\sin\alpha_{ir}\beta_{ccc},\end{aligned} \tag{9}$$

in which φ is the azimuthal rotational angle: the angle of the x-z plane with respect to the a-c around the z axis. The measured I_{sf} under ppp polarization we thus expect to simplify to (where A and B are constants that are independent of orientation)

$$I_{sf,ppp}(\omega_{sfg}) \propto |A - B\ \sin(3\varphi)|^2. \tag{10}$$

Equation (10) implies that the I_{sf} of the Ag(111) surface should have 6-fold symmetry under rotation in φ if $A \ll B$, which is the case for Ag(111).[99] As shown previously, this underlying structural symmetry is similarly revealed in the measured LEED pattern. To understand why, recall that the Bragg reflections of the LEED pattern result from the intersection of the Ewald sphere with the Ag(111) reciprocal lattice.[3] The Ag(111) surface lattice is hexagonal, and thus its reciprocal lattice is also hexagonal. Therefore, the LEED pattern of Ag(111) shows a six fold rotational symmetry.[100,101] Figure 5(a) shows the crystal structure, Fig. 5(b) (top) the azimuthal dependent VSFG signal, and Fig. 5(b) (bottom) the LEED pattern measured for the same sample. Clearly, the expected 6-fold symmetry is observed, consistent with prior work,[95,99] and the azimuthal dependent nonresonant SFG signal measured within our UHV chamber offers an all-optical probe of surface structural symmetry.[48,98,102,103]

F. Scanning SFG microscopy on Ag(111)

Having demonstrated that our UHV setup allows the measurement of azimuthal angle dependent SFG intensities, we finally demonstrate that it allows sample translation in the imaging plane with sufficient stability to image ≈10 μm sample features. As noted earlier, this capability is crucial for the study of TMDC monolayers (whose preparation typically results in ≈10 μm-sized flakes); therefore, sample characterization requires optical alignment on the sample. A silver sample with two curved lines on the surface is prepared by sputtering the same sample position with argon ions for 2 h and repeating the argon ion sputtering by translating the sample 1 mm in the direction perpendicular to the argon ion beam.

Figure 6(a) shows a point-wise scanning sum-frequency generation microscopy image of this Ag sample, obtained by translating the sample, both horizontally and vertically, in the image plane. Figure 6(b) shows an optical microscopy image of the same area of the same Ag sample. Clearly, it is possible to image the steps on the Ag surface either by wide-field visible or scanning SFG microscopy. However, because the linear optical susceptibility is a first and second order susceptibility and a second rank tensor, the potential information content of the SFG image is higher. Point-wise scanning or wide-field SFG microscopes for samples in ambient air or electrochemical environments have been reported previously.[104–107] This measurement is, to our knowledge, the first demonstration of this capability in UHV.

Since SFG is sensitive to surface adsorbates with sub-monolayer sensitivity, scanning SFG microscopy has the potential to probe the –CH, –CO, –OH, etc. vibrations and map the spatial distribution of such "fingerprint" vibrations.[104] While the current setup is optimized to spectrally resolve features that are 41 μm or larger (as required for experiments involving mechanically exfoliated TMDC samples on Au surfaces), clearly one can imagine systems in which it might be useful to image molecular organization on length scales both shorter (and longer). As discussed in the methods section, increased spatial resolution of down to 21 μm is straightforwardly achievable by a small change in the visible probe beam focusing optics. In general terms, we expect 2D heterostructures known to be heterogeneous on a length scale much larger than *single* molecular adsorbates to be promising systems to be studied by our scanning SFG microscopy. The spatially resolved performance of such heterojunction based devices has been previously described using Optical Beam Induced Current (OBIC).[108,109] OBIC utilizes a single color CW optical beam to excite the sample and collects the photocurrent of the heterojunction device by scanning the optical beam in two dimensions to map the uniformity of the local performance. Such a measurement does not offer correlated structural insight; it is difficult to understand how changes in local structure correlate with device performance. Our setup offers the straightforward possibility of combining OBIC with SFG spectromicroscopy (particularly *operando* while photocurrent is flowing[110]). Given this spatial resolution and the symmetry-enabled ability to separate the different contributions to the SFG signal, our setup seems poised to offer significant new insight into the basic physics of 2D material heterostructures.

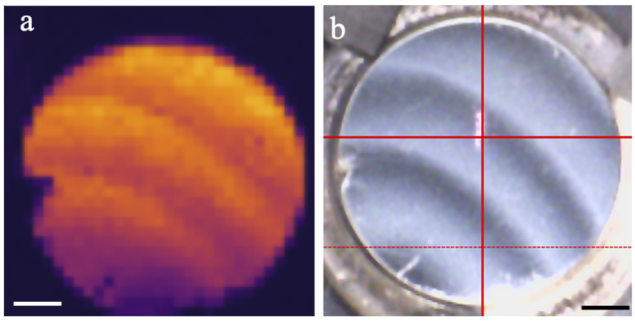

FIG. 6. (a) Scanning sum-frequency generation microscopy image of an Ag sample measured by scanning the sample horizontally and vertically. The circle in the image refers to the shape of the measured Ag sample, which is round with a diameter of ~6 mm. (b) Optical microscopy image of the same area of the same Ag sample. The scale bars represent 1 mm. See the text for details.

III. CONCLUSION

Probing interfaces between condensed phases and their non-equilibrium dynamics (e.g., time dependent ultrafast charge and energy transfer), particularly those involving stacks of two dimensional materials, is challenging. Because it is largely restricted to linear photon-in/photon-out techniques, much of the difficulty lies in separating the optical responses of either bulk phase from those of the 2D material (whether an atomically thin heterostructure or the surface state of a semiconductor). We and others have previously shown that the symmetry of the second order nonlinear susceptibility, i.e., the $\chi^{(2)}$, particularly with respect to rotation around the interface normal, offers the possibility of near quantitative separation of the optical response of different portions of the interface. Such measurements have, virtually exclusively, focused on heterostructures of solids and atomically thin 2D materials in ambient environments, making temperature control and controlled dosing of molecular condensed matter (i.e., molecular films) challenging.

We here describe a setup that overcomes this limitation: an ultra-high vacuum setup that integrates conventional surface science techniques with azimuthal and polarization dependent, femtosecond time-resolved sum frequency generation spectroscopy and scanning sum frequency generation microscopy. Polarization femtosecond resolved time-averaged vibrationally resonant SFG is demonstrated by its application to a CO monolayer on Pt(111). Because the setup allows the extraction of both the LEED pattern and the spectrum under multiple polarizations, it is possible to extract the CO interfacial hyperpolarizability ratio (i.e., $R = \frac{\beta^{(2)}_{aac}}{\beta^{(2)}_{ccc}}$) without the CO orientations assumed in previous studies. We show that the setup offers femtosecond time-resolution by measuring the so-called free induction decay of the CO stretch vibration on Pt(111), which shows that the spectral line-width measured in the time domain quantitatively reproduces that measured in the frequency domain using a spectrograph/EMICCD camera combination. The ability to record SFG signals as a function of sample azimuthal rotation is demonstrated for the Ag(111) surface. Because we measure LEED on the same sample in our UHV system, we can directly correlate the 6-fold symmetry of the nonresonant SFG response with the 6-fold symmetry of the LEED pattern. Finally, we demonstrate sufficient stability to perform scanning SFG microscopy on ≈10 μm length

scales by comparing an optical micrograph and the scanned SFG signal from an intentionally defect ridden Ag sample.

This ability to perform both SFG spectroscopy with full characterization of $\chi^{(2)}$ symmetries with femtosecond temporal resolution and spatially resolve this signal over 10 μm length scales in UHV appears to offer an important new window into the physics of two dimensional systems, whether topologically protected surface states, heterostructures of atomically thin two dimensional material, or molecular-adsorbate solid interfaces.

SUPPLEMENTARY MATERIAL

The supplementary material contains details regarding the laser parameters, LEED pattern of clean Pt(111), LEEDpat simulation, CO adsorption energy on Pt(111), hyperpolarizability ratio of CO on Pt(111), and free induction decay time constant fit model.

ACKNOWLEDGMENTS

We want to acknowledge H. Kirsch and S. Kubala for their valuable discussions regarding the initial design of the setup. We acknowledge M. Lackner for his help in developing the control software for the setup and E. Hasselbrink for donating his LEED/AES device. This work was supported by the Deutsche Forschungsgemeinschaft (DFG, German Research Foundation) through Projects A06 of the Collaborative Research Center SFB 1242, "Non-Equilibrium Dynamics of Condensed Matter in the Time Domain" (Project No. 278162697), through Germany's Excellence Strategy (Grant No. EXC 2033-390677874-RESOLV), and through SCHL 384/20-1 (Project No. 406129719). Additional support was provided by the European Research Council, i.e., ERC-CoG-2017 SOLWET (Project No. 772286), to R.K.C.

AUTHOR DECLARATIONS

Conflict of Interest

The authors have no conflicts to disclose.

Author Contributions

Zhipeng Huang: Data curation (equal); Formal analysis (lead); Investigation (lead); Methodology (equal); Validation (equal); Visualization (lead); Writing – original draft (lead); Writing – review & editing (equal). **Tobias Roos**: Investigation (equal); Methodology (equal); Resources (equal). **Yujin Tong**: Formal analysis (equal); Funding acquisition (equal); Investigation (equal); Methodology (equal); Project administration (equal); Supervision (equal); Validation (equal); Writing – original draft (equal); Writing – review & editing (equal). **R. Kramer Campen**: Conceptualization (equal); Formal analysis (equal); Funding acquisition (lead); Investigation (equal); Project administration (lead); Supervision (lead); Validation (equal); Writing – original draft (equal); Writing – review & editing (lead).

DATA AVAILABILITY

The data that support the findings of this study are available from the corresponding author upon reasonable request.

REFERENCES

[1]S. R. Bare and G. A. Somorjai, "Surface chemistry," in *Encyclopedia of Physical Science and Technology*, 3rd ed. (Academic Press, 2003), pp. 373–421.
[2]J. L. Bañuelos, E. Borguet, G. E. Brown, R. T. Cygan, J. J. DeYoreo, P. M. Dove, M.-P. Gaigeot, F. M. Geiger, J. M. Gibbs, V. H. Grassian, A. G. Ilgen, Y.-S. Jun, N. Kabengi, L. Katz, J. D. Kubicki, J. Lützenkirchen, C. V. Putnis, R. C. Remsing, K. M. Rosso, G. Rother, M. Sulpizi, M. Villalobos, and H. Zhang, "Oxide- and silicate-water interfaces and their roles in technology and the environment," Chem. Rev. **123**, 6413–6544 (2023).
[3]M. V. Hove, W. Weinberg, and C.-M. Chan, *Low-Energy Electron Diffraction: Experiment, Theory, and Surface Structure Determination* (Springer, 1986).
[4]C. C. Chang, "Auger electron spectroscopy," Surf. Sci. **25**, 53–79 (1971).
[5]F. Hofer, F. P. Schmidt, W. Grogger, and G. Kothleitner, "Fundamentals of electron energy-loss spectroscopy," IOP Conf. Ser.: Mater. Sci. Eng. **109**, 012007 (2016).
[6]D. A. King, "Thermal desorption from metal surfaces: A review," Surf. Sci. **47**, 384–402 (1975).
[7]B. Holst, G. Alexandrowicz, N. Avidor, G. Benedek, G. Bracco, W. E. Ernst, D. Farías, A. P. Jardine, K. Lefmann, J. R. Manson, R. Marquardt, S. M. Artés, S. J. Sibener, J. W. Wells, A. Tamtögl, and W. Allison, "Material properties particularly suited to be measured with helium scattering: Selected examples from 2D materials, van der Waals heterostructures, glassy materials, catalytic substrates, topological insulators and superconducting radio frequency materials," Phys. Chem. Chem. Phys. **23**, 7653–7672 (2021).
[8]C. Yang and C. Wöll, "IR spectroscopy applied to metal oxide surfaces: Adsorbate vibrations and beyond," Adv. Phys.: X **2**, 373–408 (2017).
[9]J. D. Kestell, K. Mudiyanselage, X. Ye, C.-Y. Nam, D. Stacchiola, J. Sadowski, and J. A. Boscoboinik, "Stand-alone polarization-modulation infrared reflection absorption spectroscopy instrument optimized for the study of catalytic processes at elevated pressures," Rev. Sci. Instrum. **88**, 105109 (2017).
[10]L. A. Bottomley, J. E. Coury, and P. N. First, "Scanning probe microscopy," Anal. Chem. **68**, 185R–230R (1996).
[11]E. H. G. Backus, A. Eichler, A. W. Kleyn, and M. Bonn, "Real-time observation of molecular motion on a surface," Science **310**, 1790–1793 (2005).
[12]S. Vogelgesang, G. Storeck, J. G. Horstmann, T. Diekmann, M. Sivis, S. Schramm, K. Rossnagel, S. Schäfer, and C. Ropers, "Phase ordering of charge density waves traced by ultrafast low-energy electron diffraction," Nat. Phys. **14**, 184–190 (2018).
[13]G. Storeck, K. Rossnagel, and C. Ropers, "Ultrafast spot-profile LEED of a charge-density wave phase transition," Appl. Phys. Lett. **118**, 221603 (2021).
[14]R. Schlögl, "Heterogeneous catalysis," Angew. Chem., Int. Ed. **54**, 3465–3520 (2015).
[15]F. Zaera, "Probing liquid/solid interfaces at the molecular level," Chem. Rev. **112**, 2920–2986 (2012).
[16]Y. R. Shen, "Surface properties probed by second-harmonic and sum-frequency generation," Nature **337**, 519–525 (1989).
[17]Q. Du, R. Superfine, E. Freysz, and Y. R. Shen, "Vibrational spectroscopy of water at the vapor/water interface," Phys. Rev. Lett. **70**, 2313–2316 (1993).
[18]Q. Du, E. Freysz, and Y. R. Shen, "Vibrational spectra of water molecules at quartz/water interfaces," Phys. Rev. Lett. **72**, 238–241 (1994).
[19]S. Yamaguchi and T. Tahara, "Development of electronic sum frequency generation spectroscopies and their application to liquid interfaces," J. Phys. Chem. C **119**, 14815–14828 (2015).
[20]M. Roiaz, V. Pramhaas, X. Li, C. Rameshan, and G. Rupprechter, "Atmospheric pressure reaction cell for operando sum frequency generation spectroscopy of ultrahigh vacuum grown model catalysts," Rev. Sci. Instrum. **89**, 045104 (2018).
[21]X. Li, V. Pramhaas, C. Rameshan, P. Blaha, and G. Rupprechter, "Coverage-induced orientation change: CO on Ir(111) monitored by polarization-dependent sum frequency generation spectroscopy and density functional theory," J. Phys. Chem. C **124**, 18102–18111 (2020).
[22]M. Bonn, C. Hess, S. Funk, J. H. Miners, B. N. Persson, M. Wolf, and G. Ertl, "Femtosecond surface vibrational spectroscopy of CO adsorbed on Ru(001) during desorption," Phys. Rev. Lett. **84**, 4653–4656 (2000).
[23]For practical considerations–sensitive Si-based detector are widely available for light at visible wavelengths while detectors in for near-infrared wavelengths are

generally less sensitive–the great majority of reported second order nonlinear optical spectroscopy employs a sum (and not difference) frequency approach. To aid in concise exposition we therefore refer only to SFG going forward, although similar insights are, in principle, available from DFG.
[24]X. Zhuang, P. B. Miranda, D. Kim, and Y. R. Shen, "Mapping molecular orientation and conformation at interfaces by surface nonlinear optics," Phys. Rev. B **59**, 12632–12640 (1999).
[25]X. Wei and Y. R. Shen, "Motional effect in surface sum-frequency vibrational spectroscopy," Phys. Rev. Lett. **86**, 4799–4802 (2001).
[26]A. G. Lambert, P. B. Davies, and D. J. Neivandt, "Implementing the theory of sum frequency generation vibrational spectroscopy: A tutorial review," Appl. Spectrosc. Rev. **40**, 103–145 (2005).
[27]H. F. Wang, W. Gan, R. Lu, Y. Rao, and B. H. Wu, "Quantitative spectral and orientational analysis in surface sum frequency generation vibrational spectroscopy (SFG-VS)," Int. Rev. Phys. Chem. **24**, 191–256 (2005).
[28]W.-T. Liu and Y. R. Shen, "Surface vibrational modes of α-quartz(0001) probed by sum-frequency spectroscopy," Phys. Rev. Lett. **101**, 016101 (2008).
[29]W.-T. Liu and Y. R. Shen, "Sum-frequency phonon spectroscopy on α-quartz," Phys. Rev. B **78**, 024302 (2008).
[30]J. M. Lantz and R. M. Corn, "Electrostatic field measurements and band flattening during electron-transfer processes at single-crystal TiO_2 electrodes by electric field-induced optical second harmonic generation," J. Phys. Chem. **98**, 4899–4905 (1994).
[31]S. Ong, X. Zhao, and K. B. Eisenthal, "Polarization of water molecules at a charged interface: Second harmonic studies of the silica/water interface," Chem. Phys. Lett. **191**, 327–335 (1992).
[32]F. M. Geiger, "Second harmonic generation, sum frequency generation, and $\chi^{(3)}$: Dissecting environmental interfaces with a nonlinear optical Swiss army knife," Annu. Rev. Phys. Chem. **60**, 61–83 (2009).
[33]Y.-C. Wen, S. Zha, X. Liu, S. Yang, P. Guo, G. Shi, H. Fang, Y. R. Shen, and C. Tian, "Unveiling microscopic structures of charged water interfaces by surface-specific vibrational spectroscopy," Phys. Rev. Lett. **116**, 016101 (2016).
[34]P. E. Ohno, H. f. Wang, and F. M. Geiger, "Second-order spectral lineshapes from charged interfaces," Nat. Commun. **8**, 1032 (2017).
[35]M. Zeng, Y. Xiao, J. Liu, K. Yang, and L. Fu, "Exploring two-dimensional materials toward the next-generation circuits: From monomer design to assembly control," Chem. Rev. **118**, 6236–6296 (2018).
[36]V. Shanmugam, R. A. Mensah, K. Babu, S. Gawusu, A. Chanda, Y. Tu, R. E. Neisiany, M. Försth, G. Sas, and O. Das, "A review of the synthesis, properties, and applications of 2D materials," Part. Part. Syst. Charact. **39**, 2200031 (2022).
[37]P. Kumbhakar, J. S. Jayan, A. Sreedevi Madhavikutty, P. R. Sreeram, A. Saritha, T. Ito, and C. S. Tiwary, "Prospective applications of two-dimensional materials beyond laboratory frontiers: A review," iScience **26**, 106671 (2023).
[38]J. F. Sierra, J. Fabian, R. K. Kawakami, S. Roche, and S. O. Valenzuela, "Van der Waals heterostructures for spintronics and opto-spintronics," Nat. Nanotechnol. **16**, 856–868 (2021).
[39]F. He, Y. Zhou, Z. Ye, S.-H. Cho, J. Jeong, X. Meng, and Y. Wang, "Moiré patterns in 2D materials: A review," ACS Nano **15**, 5944–5958 (2021).
[40]S. K. Behura, A. Miranda, S. Nayak, K. Johnson, P. Das, and N. R. Pradhan, "Moiré physics in twisted van der Waals heterostructures of 2D materials," Emergent Mater. **4**, 813–826 (2021).
[41]S. Park, N. Mutz, T. Schultz, S. Blumstengel, A. Han, A. Aljarb, L.-J. Li, E. J. W. List-Kratochvil, P. Amsalem, and N. Koch, "Direct determination of monolayer MoS_2 and WSe_2 exciton binding energies on insulating and metallic substrates," 2D Mater. **5**, 025003 (2018).
[42]E. Pollmann, S. Sleziona, T. Foller, U. Hagemann, C. Gorynski, O. Petri, L. Madauß, L. Breuer, and M. Schleberger, "Large-area, two-dimensional MoS_2 exfoliated on gold: Direct experimental access to the metal-semiconductor interface," ACS Omega **6**, 15929–15939 (2021).
[43]Y. Wang, J. Xiao, S. Yang, Y. Wang, and X. Zhang, "Second harmonic generation spectroscopy on two-dimensional materials [Invited]," Opt. Mater. Express **9**, 1136–1149 (2019).
[44]J. Zhang, W. Zhao, P. Yu, G. Yang, and Z. Liu, "Second harmonic generation in 2D layered materials," 2D Mater. **7**, 042002 (2020).
[45]Y. Li, Y. Rao, K. F. Mak, Y. You, S. Wang, C. R. Dean, and T. F. Heinz, "Probing symmetry properties of few-layer MoS_2 and h-BN by optical second-harmonic generation," Nano Lett. **13**, 3329–3333 (2013).
[46]A. R. Khan, B. Liu, T. Lü, L. Zhang, A. Sharma, Y. Zhu, W. Ma, and Y. Lu, "Direct measurement of folding angle and strain vector in atomically thin WS_2 using second-harmonic generation," ACS Nano **14**, 15806–15815 (2020).
[47]Y. V. Zhumagulov, V. D. Neverov, A. E. Lukyanov, D. R. Gulevich, A. V. Krasavin, A. Vagov, and V. Perebeinos, "Nonlinear spectroscopy of excitonic states in transition metal dichalcogenides," Phys. Rev. B **105**, 115436 (2022).
[48]T. Yang, E. Pollmann, S. Sleziona, E. Hasselbrink, P. Kratzer, M. Schleberger, R. K. Campen, and Y. Tong, "Interaction between a gold substrate and monolayer MoS_2: An azimuthal-dependent sum frequency generation study," Phys. Rev. B **107**, 155433 (2023).
[49]T. Yang, S. Sleziona, E. Pollmann, E. Hasselbrink, P. Kratzer, M. Schleberger, R. K. Campen, and Y. Tong, "Isolating the optical response of a MoS_2 monolayer under extreme screening of a metal substrate," Phys. Rev. B **109**, L161402 (2024).
[50]P. Rivera, K. L. Seyler, H. Yu, J. R. Schaibley, J. Yan, D. G. Mandrus, W. Yao, and X. Xu, "Valley-polarized exciton dynamics in a 2D semiconductor heterostructure," Science **351**, 688–691 (2016).
[51]S. Ulstrup, A. G. Čabo, D. Biswas, J. M. Riley, M. Dendzik, C. E. Sanders, M. Bianchi, C. Cacho, D. Matselyukh, R. T. Chapman, E. Springate, P. D. C. King, J. A. Miwa, and P. Hofmann, "Spin and valley control of free carriers in single-layer WS_2," Phys. Rev. B **95**, 041405 (2017).
[52]R. Austin, Y. R. Farah, T. Sayer, B. M. Luther, A. Montoya-Castillo, A. T. Krummel, and J. B. Sambur, "Hot carrier extraction from 2D semiconductor photoelectrodes," Proc. Natl. Acad. Sci. U. S. A. **120**, e2220333120 (2023).
[53]G. D. Boyd and D. A. Kleinman, "Parametric interaction of focused Gaussian light beams," J. Appl. Phys. **39**, 3597–3639 (1968).
[54]W. Seka, S. D. Jacobs, J. E. Rizzo, R. Boni, and R. S. Craxton, "Demonstration of high efficiency third harmonic conversion of high power Nd-glass laser radiation," Opt. Commun. **34**, 469–473 (1980).
[55]R. Hui and M. O'Sullivan, "Basic mechanisms and instrumentation for optical measurement," in *Fiber-Optic Measurement Techniques*, 2nd ed. (Academic Press, 2023), pp. 137–295.
[56]G. Zwaschka, M. Wolf, R. K. Campen, and Y. Tong, "A microscopic model of the electrochemical vibrational Stark effect: Understanding VSF spectroscopy of (bi)sulfate on Pt(111)," Surf. Sci. **678**, 78–85 (2018).
[57]H.-J. Freund, G. Meijer, M. Scheffler, R. Schlögl, and M. Wolf, "CO oxidation as a prototypical reaction for heterogeneous processes," Angew. Chem., Int. Ed. **50**, 10064–10094 (2011).
[58]H. Bae, C. Seong, V. Burungale, M. Seol, C. O. Yoon, S. H. Kang, W.-G. Jung, B.-J. Kim, and J.-S. Ha, "Nanostructured Au electrode with 100 h stability for solar-driven electrochemical reduction of carbon dioxide to carbon monoxide," ACS Omega **7**, 9422–9429 (2022).
[59]G. Ertl, M. Neumann, and K. M. Streit, "Chemisorption of CO on the Pt(111) surface," Surf. Sci. **64**, 393–410 (1977).
[60]H. Steininger, S. Lehwald, and H. Ibach, "On the adsorption of CO on Pt(111)," Surf. Sci. **123**, 264–282 (1982).
[61]The pumping speed of the HiPace 700 H turbomolecular pump is 685 l/s for N_2.
[62]M. Polanyi and E. Wigner, "Bildung und zerfall von molekülen," Z. Phys. **33**, 429–434 (1925).
[63]A. M. de Jong and J. W. Niemantsverdriet, "Thermal desorption analysis: Comparative test of ten commonly applied procedures," Surf. Sci. **233**, 355–365 (1990).
[64]P. R. Norton, J. A. Davies, and T. E. Jackman, "Absolute coverages of CO and O on Pt(111); comparison of saturation CO coverages on Pt(100), (110) and (111) surfaces," Surf. Sci. Lett. **122**, L593–L600 (1982).
[65]K. Hermann and M. A. v. Hove, LEEDpat Download Package, 2022.
[66]M. Maglietta, F. Pratesi, and G. Rovida, "Quantitative determination of carbon on silver by Auger spectroscopy," Chem. Phys. Lett. **36**, 436–440 (1975).
[67]A. M. Bradshaw and J. Pritchard, "Infrared spectra of carbon monoxide chemisorbed on metal films: A comparative study of copper, silver, gold, iron, cobalt and nickel," Proc. R. Soc. London, Ser. A **316**, 169–183 (1970).
[68]M. Trenary, "Reflection absorption infrared spectroscopy and the structure of molecular adsorbates on metal surfaces," Annu. Rev. Phys. Chem. **51**, 381–403 (2000).

[69]X. Li, M. Roiaz, V. Pramhaas, C. Rameshan, and G. Rupprechter, "Polarization-dependent SFG spectroscopy of near ambient pressure CO adsorption on Pt(111) and Pd(111) revisited," Top. Catal. **61**, 751–762 (2018).
[70]C. Hirose, N. Akamatsu, and K. Domen, "Formulas for the analysis of the surface SFG spectrum and transformation coefficients of cartesian SFG tensor components," Appl. Spectrosc. **46**, 1051–1072 (1992).
[71]G. Apai, P. S. Wehner, R. S. Williams, J. Stohr, and D. A. Shirley, "Orientation of CO on Pt(111) and Ni(111) surfaces from angle-resolved photoemission," Phys. Rev. Lett. **37**, 1497–1500 (1976).
[72]P. Hofmann, S. R. Bare, N. V. Richardson, and D. A. King, "Orientation of chemisorbed species from orthogonal-plane arups: Tilted CO on Pt{110} and upright CO on Pt{111}," Solid State Commun. **42**, 645–651 (1982).
[73]D. A. Wesner, F. P. Coenen, and H. P. Bonzel, "Orientation of adsorbed CO on Pt(111) + K by x-ray photoelectron diffraction," Phys. Rev. B **33**, 8837–8840 (1986).
[74]D. F. Ogletree, M. A. Van Hove, and G. A. Somorjai, "LEED intensity analysis of the structures of clean Pt(111) and of CO adsorbed on Pt(111) in the c(4 × 2) arrangement," Surf. Sci. **173**, 351–365 (1986).
[75]B. Busson and A. Tadjeddine, "Non-uniqueness of parameters extracted from resonant second-order nonlinear optical spectroscopies," J. Phys. Chem. C **113**, 21895–21902 (2009).
[76]D. K. Lambert, "Vibrational Stark effect of adsorbates at electrochemical interfaces," Electrochim. Acta **41**, 623–630 (1996).
[77]S. J. A. van Gisbergen, J. G. Snijders, and E. J. Baerends, "Accurate density functional calculations on frequency-dependent hyperpolarizabilities of small molecules," J. Chem. Phys. **109**, 10657–10668 (1998).
[78]S. Baldelli, N. Markovic, P. Ross, Y.-R. Shen, and G. Somorjai, "Sum frequency generation of CO on (111) and polycrystalline platinum electrode surfaces: Evidence for SFG invisible surface CO," J. Phys. Chem. B **103**, 8920–8925 (1999).
[79]A. Ouvrard, J. Wang, A. Ghalgaoui, S. Nave, S. Carrez, W. Zheng, H. Dubost, and B. Bourguignon, "CO adsorption on Pd(100) revisited by sum frequency generation: Evidence for two adsorption sites in the compression stage," J. Phys. Chem. C **118**, 19688–19700 (2014).
[80]Y. Tong, "Linear vs. nonlinear electrochemical vibrational Stark effect: Preconditions of the approximation," in *Encyclopedia of Solid-Liquid Interfaces*, 1st ed., edited by K. Wandelt and G. Bussetti (Elsevier, Oxford, 2024), pp. 750–759.
[81]C. Klünker, M. Balden, S. Lehwald, and W. Daum, "CO stretching vibrations on Pt(111) and Pt(110) studied by sumfrequency generation," Surf. Sci. **360**, 104–111 (1996).
[82]W. G. Roeterdink, M. Bonn, and R. A. Olsen, "The CO–H interaction on Pt(111) studied using temperature programmed vibrational sum frequency generation," Chem. Phys. Lett. **412**, 482–487 (2005).
[83]F. Fournier, W. Zheng, S. Carrez, H. Dubost, and B. Bourguignon, "Ultrafast laser excitation of CO/Pt(111) probed by sum frequency generation: Coverage dependent desorption efficiency," Phys. Rev. Lett. **92**, 216102 (2004).
[84]E. H. G. Backus, M. Forsblom, M. Persson, and M. Bonn, "Highly efficient ultrafast energy transfer into molecules at surface step sites," J. Phys. Chem. C **111**, 6149–6153 (2007).
[85]M. Nagao, K. Watanabe, and Y. Matsumoto, "Ultrafast vibrational energy transfer in the layers of D_2O and CO on Pt(111) studied with time-resolved sum-frequency-generation spectroscopy," J. Phys. Chem. C **113**, 11712–11719 (2009).
[86]H. Arnolds and M. Bonn, "Ultrafast surface vibrational dynamics," Surf. Sci. Rep. **65**, 45–66 (2010).
[87]M. Wolf, "Femtosecond dynamics of electronic excitations at metal surfaces," Surf. Sci. **377–379**, 343–349 (1997).
[88]J. D. Beckerle, R. R. Cavanagh, M. P. Casassa, E. J. Heilweil, and J. C. Stephenson, "Subpicosecond transient infrared spectroscopy of adsorbates. Vibrational dynamics of CO/Pt(111)," J. Chem. Phys. **95**, 5403–5418 (1991).
[89]S. Roke, A. W. Kleyn, and M. Bonn, "Time- vs. frequency-domain femtosecond surface sum frequency generation," Chem. Phys. Lett. **370**, 227–232 (2003).
[90]C. S. Ponseca, Jr., P. Chábera, J. Uhlig, P. Persson, and V. Sundström, "Ultrafast electron dynamics in solar energy conversion," Chem. Rev. **117**, 10940–11024 (2017).
[91]H. Frei, "Time-resolved vibrational and electronic spectroscopy for understanding how charges drive metal oxide catalysts for water oxidation," J. Phys. Chem. Lett. **13**, 7953–7964 (2022).
[92]C. Wen, A. Yin, and W.-L. Dai, "Recent advances in silver-based heterogeneous catalysts for green chemistry processes," Appl. Catal., B **160-161**, 730–741 (2014).
[93]C. Li and X. Bi, *Silver Catalysis in Organic Synthesis* (Wiley-VCH Verlag GmbH and Co. KGaA, 2019).
[94]I.-K. Suh, H. Ohta, and Y. Waseda, "High-temperature thermal expansion of six metallic elements measured by dilatation method and X-ray diffraction," J. Mater. Sci. **23**, 757–760 (1988).
[95]K. A. Friedrich and G. L. Richmond, "Surface second harmonic generation studies of stepped Ag (111) electrode surfaces," Chem. Phys. Lett. **213**, 491–497 (1993).
[96]H. A. Engelhardt and D. Menzel, "Adsorption of oxygen on silver single crystal surfaces," Surf. Sci. **57**, 591–618 (1976).
[97]M. Chelvayohan and C. H. B. Mee, "Work function measurements on (110), (100) and (111) surfaces of silver," J. Phys. C: Solid State Phys. **15**, 2305–2312 (1982).
[98]R. W. Boyd, *Nonlinear Optics*, 4th ed. (Academic Press, 2020).
[99]A. L. Harris, L. Rothberg, L. Dhar, N. J. Levinos, and L. H. Dubois, "Vibrational energy relaxation of a polyatomic adsorbate on a metal surface: Methyl thiolate (CH_3S) on Ag(111)," J. Chem. Phys. **94**, 2438–2448 (1991).
[100]E. A. Soares, V. B. Nascimento, V. E. de Carvalho, C. M. C. de Castilho, A. V. de Carvalho, R. Toomes, and D. P. Woodruff, "Structure determination of Ag(111) by low-energy electron diffraction," Surf. Sci. **419**, 89–96 (1999).
[101]E. A. Soares, G. S. Leatherman, R. D. Diehl, and M. A. Van Hove, "Low-energy electron diffraction study of the thermal expansion of Ag(111)," Surf. Sci. **468**, 129–136 (2000).
[102]S. K. Shaw, A. Lagutchev, D. D. Dlott, and A. A. Gewirth, "Sum-frequency spectroscopy of molecular adsorbates on low-index Ag surfaces: Effects of azimuthal rotation," Anal. Chem. **81**, 1154–1161 (2009).
[103]X. Chen, C. M. Lee, H.-F. Wang, L. Jensen, and S. H. Kim, "Experimental and theoretical study of azimuth angle and polarization dependences of sum-frequency-generation vibrational spectral features of uniaxially aligned cellulose crystals," J. Phys. Chem. C **121**, 18876–18886 (2017).
[104]A. Hanninen, M. W. Shu, and E. O. Potma, "Hyperspectral imaging with laser-scanning sum-frequency generation microscopy," Biomed. Opt. Express **8**, 4230–4242 (2017).
[105]D. Zheng, L. Lu, K. F. Kelly, and S. Baldelli, "Chemical imaging of self-assembled monolayers on copper using compressive hyperspectral sum frequency generation microscopy," J. Phys. Chem. B **122**, 464–471 (2018).
[106]G. Zwaschka, I. Nahalka, A. Marchioro, Y. Tong, S. Roke, and R. K. Campen, "Imaging the heterogeneity of the oxygen evolution reaction on gold electrodes operando: Activity is highly local," ACS Catal. **10**, 6084–6093 (2020).
[107]H. Li, K. F. Kelly, and S. Baldelli, "Spectroscopic imaging of surfaces—Sum frequency generation microscopy (SFGM) combined with compressive sensing (CS) technique," J. Chem. Phys. **153**, 190901 (2020).
[108]D. J. Dick, A. J. Heeger, Y. Yang, and Q. Pei, "Imaging the structure of the p-n junction in polymer light-emitting electrochemical cells," Adv. Mater. **8**, 985–987 (1996).
[109]G. Y. Zhuo, S. Banik, F. J. Kao, G. A. Ahmed, N. M. Kakoty, N. Mazumder, and A. Gogoi, "An insight into optical beam induced current microscopy: Concepts and applications," Microsc. Res. Tech. **85**, 3495–3513 (2022).
[110]Z. Huang, M. Bridger, O. A. Naranjo-Montoya, A. Tarasevitch, U. Bovensiepen, Y. Tong, and R. K. Campen, "A femtosecond time resolved view of vibrationally assisted electron transfer across the metal/aqueous interface," arXiv:2304.06684 [physics] (2023).